Original Article
Three-dimensional visualization of Hertwig's epithelial root sheath during tooth root development with the miniTESOS tissue clearing method

Jiayu Wang*, Miao Yu*, Yang Liu, Dong Han

Department of Prosthodontics, Peking University School and Hospital of Stomatology & National Center for Stomatology & National Clinical Research Center for Oral Diseases & National Engineering Research Center of Oral Biomaterials and Digital Medical Devices & Central Laboratory, Peking University School and Hospital of Stomatology, No. 22 Zhongguancun South Avenue, Haidian District, Beijing 100081, PR China. *Equal contributors.

Abstract: Objective: Hertwig's epithelial root sheath (HERS) acts as a signaling center that regulates the size, shape, and number of tooth roots. Therefore, understanding the anatomical changes in HERS during development is crucial for investigating its effect on root formation. However, the three-dimensional morphology of HERS and its changes during tooth root development remain largely unknown due to the limitations of traditional histological techniques. Methods: We developed an improved tissue clearing method for mouse embryonic and early postnatal mandibles, designated as a mini Transparent Embedding Solvent System (miniTESOS), based on the Transparent Embedding Solvent System (TESOS). We applied this method to the *K14-Cre;Ai14* mouse line to systematically investigate the spatiotemporal dynamics of HERS at the cellular level during the development of the roots of mandibular first molars (MM1) and mandibular second molars (MM2). Additionally, using MM1 as a model, we quantitatively investigated the spatiotemporal changes in HERS in the root bifurcation region during the development of two-rooted teeth. Results: In the early stages of root development, differences in growth rates and developmental patterns between MM1 and MM2 were observed in the mesiodistal and buccolingual directions, from the initiation to the fusion of buccal and lingual HERS. In the elongation stage of two-rooted teeth, continuous HERS was found exclusively at the leading edge of the root, gradually decreasing in length as the root extended. In the root bifurcation area, HERS undergoes four developmental stages: initiation, elongation, contact, and complete fragmentation, each characterized by specific morphological features. Conclusion: This study improves the understanding of the alterations in HERS during root development and summarizes its developmental pattern in the root bifurcation region. The miniTESOS tissue clearing method provides a new strategy to investigate tooth development.

Keywords: Hertwig's epithelial root sheath, tooth root development, tissue clearing, TESOS, miniTESOS, three-dimensional imaging

Introduction

Teeth serve as an ideal model for investigating the molecular mechanisms of organ development, allowing for indispensable research on embryonic morphogenesis, adult tissue regeneration, and stem cell biology [1]. The tooth root, situated beneath the crown and embedded in the jawbone, provides essential support for chewing and occlusion, while also maintaining the alignment and integrity of the dental arch [2]. Study has consistently linked tooth root development with Hertwig's epithelial root sheath (HERS) [3], a bilayered epithelial cell sheath consisting of inner and outer enamel epithelium extending apically from the cervical loop [4]. Throughout tooth root development, HERS functions as a signaling center, influencing the size, shape, and number of tooth roots, highlighting its critical role in root formation [5]. As root development advances, HERS progressively disintegrates to form the epithelial rests of Malassez (ERM) [6], indicating its transient nature. Therefore, understanding the anatomi-

cal changes in HERS during tooth root development is crucial for understanding its role in root morphogenesis. However, due to methodological limitations, the three-dimensional morphology of HERS remains largely unexplored.

In studies on tooth development, a crucial aspect of understanding the behavior and molecular mechanisms of tooth root development lies in establishing reliable models of HERS morphology [7]. As HERS is a non-mineralized soft tissue, traditional imaging techniques, such as micro-computed tomography (micro-CT), are unable to reveal its morphology at high resolution [8]. Histological sectioning is the primary method for observing HERS morphology. However, inconsistencies in sectioning angles across samples can lead to variations in observed morphology, introducing potential unreliability in observations [9]. While efforts have been made to reconstruct three-dimensional images of tooth epithelium from continuous histological sections, this approach requires highly intact and continuous tissue sections, posing challenges in visualizing cellular components and using fluorescent markers. Moreover, ensuring adequate resolution and accuracy in the reconstructed tissue images remains problematic [10]. Therefore, comprehensively and precisely visualizing the spatial morphology of HERS is a major challenge.

Information on spatial organization is crucial for understanding the complexity of biological structures and their development. Recently, tissue clearing has emerged as an effective technique in neuroscience [11, 12]. Biological tissues typically limit optical imaging depth due to their propensity to scatter and absorb photons [13]. Tissue clearing, however, overcomes this obstacle by rendering tissues transparent, thus enabling deep imaging capabilities. This technological leap greatly improves our ability to study biological tissues by facilitating enhanced visualization and analysis [14]. The process involves steps such as decolorization, decalcification, and delipidation, which collectively remove opaque elements from tissue samples, allowing greater light penetration [15]. Subsequently, these cleared tissues are examined by imaging techniques such as light-sheet or confocal microscopy, providing high-resolution images of tissue structures [16]. Tissue clearing technology holds immense potential

across scientific disciplines. For example, in developmental biology, it allows researchers to track the spatiotemporal dynamics of organogenesis with exceptional clarity [17, 18]. Recently, a new tissue clearing technique known as Transparent Embedding Solvent System (TESOS) has emerged. This cost-effective and time-efficient method achieves uniform transparency while preserving endogenous fluorescence [19]. TESOS enables direct observation of fluorescence signals within tissues using different fluorescence microscopes, thus providing new ways to describe and quantitatively analyze the relationship between tooth root development and the structure of HERS.

In this study, we introduced a novel miniTESOS method based on TESOS tissue clearing technology, customized for mouse embryonic and early postnatal mandibles, offering reduced clearing time. Using the *K14-Cre;Ai14* mouse line for specific epithelial cell labeling, we systematically investigated the spatiotemporal dynamics of tooth germ and root development by performing tissue clearing. We focused on determining the spatiotemporal changes in HERS during the development of two-rooted teeth. In the root bifurcation area, the development of HERS progresses through four stages: initiation, elongation, contact, and complete fragmentation, each characterized by distinct morphological features.

Materials and methods

Mouse strains

We generated *K14-Cre;Ai14* mice by crossing *K14-Cre* (JAX 018964) mice with *Ai14* mice (JAX 007908). Mice were obtained at embryonic days 13.5 (E13.5), 15.5 (E15.5), and 16.5 (E16.5), and postnatal days 0.5 (PN0.5), 4.5 (PN4.5), 6.5 (PN6.5), 8.5 (PN8.5), 10.5 (PN10.5), 12.5 (PN12.5), 14.5 (PN14.5), one month, and five months. Genotyping of mouse samples was performed using a One Step Mouse Genotyping Kit (Vazyme, Nanjing, China) by conducting PCR assays for both *K14-Cre* and *Ai14* transgenic mice. All mouse experiments adhered strictly to animal care and use guidelines and were approved by the Ethics Committee of the Peking University Health Science Center (LA2022177).

MiniTESOS tissue clearing method

We optimized the sample processing protocol for embryonic and early postnatal mouse mandibles using TESOS technology [19] and developed a standardized and efficient tissue clearing technique designated as miniTESOS. For embryos between E13.5 and E16.5, pregnant mice were deeply anesthetized with 5% isoflurane on the appropriate gestational days to minimize suffering, followed by perfusion. After washing with 0.02% heparin-PBS (w/v) and 4% paraformaldehyde (PFA) to clear blood vessels around the placenta, mandibles were dissected and fixed in 4% PFA for 3 h at room temperature. Then, the mandibles underwent decolorization with 25% (w/v in H_2O) Quadrol (Sigma-Aldrich, 122262) for 30 min at 37°C with shaking. Subsequently, they were sequentially incubated in tert-butanol (tB, Sigma-Aldrich, 360538) gradient solutions: 30% tB solution (composed of 70% v/v H_2O, 30% v/v tB, and 5% w/v Quadrol) and 70% tB solution (composed of 30% v/v H_2O, 70% v/v tB, and 5% w/v Quadrol), each for 30 min at 37°C with shaking. Following tissue delipidation, the mandibles were dehydrated in a tB-Q dehydration medium (composed of 70% (v/v) tB and 30% (w/v) Quadrol) for 20 min at 37°C with shaking. Next, the samples were immersed in benzylbenzoate (BB) - bisphenol A ethoxylate diacrylate (BED) clearing medium (Refractive Index (RI) = 1.552) containing 47% (v/v) BB (Sigma-Aldrich, W213802), 48% (v/v) BED (Sigma-Aldrich, 413550), 5% (w/v) Quadrol, and 2% (w/v) UV initiator Irgacure 2959 (2-Hydroxy-4'-(2-hydroxyethoxy)-2-methylpropiophenone, Sigma-Aldrich, 410896). Throughout the process, the volume of clearing reagents used was three times that of the sample volume to ensure complete immersion of the tissue sample. The samples were then covered with a coverslip. The mold was placed on ice and irradiated with UV curing light to polymerize the samples. These samples were preserved in the tube at room temperature for storage and imaging. To obtain the mandibles of early postnatal mice ranging from PN0.5 to PN14.5, mice were quickly and humanely euthanized by cervical dislocation using a guillotine. An additional step of decalcification with 0.5 M Ethylenediaminetetraacetic acid (EDTA) solution at 37°C was included between the 4% PFA fixation and decolorization steps. Specifically, the decalcification time was 30 min for PN0.5 mice and extended to three days for PN14.5 mice.

TESOS tissue clearing method

TESOS was applied to the mandibles of one-month-old and five-month-old mice following established methods [19]. Mice were first painlessly and deeply anesthetized with 5% isoflurane, and then perfused with 50 mL of 0.02% heparin-PBS (w/v), followed by 30 mL of 4% PFA for fixation. These mandibles were then fixed overnight in 4% PFA at room temperature and subsequently decalcified in 0.5 M EDTA solution at 37°C for one week. After decalcification, the mandibles underwent decolorization by incubating with a 25% (w/v in H_2O) Quadrol solution for two days at 37°C. Delipidation was performed using graded tert-butanol (tB) solutions: 30% tB solution (composed of 70% v/v water, 30% v/v tB, and 5% w/v Quadrol) for one day, 50% tB solution (composed of 50% v/v water, 50% v/v tB, and 5% w/v Quadrol) for one day, and 70% tB solution (composed of 30% v/v water, 70% v/v tB, and 5% w/v Quadrol) for one day, all at 37°C. Following delipidation, the samples were dehydrated in the tB-Q dehydration medium containing 70% v/v tB and 30% w/v Quadrol. Finally, the specimens were embedded in BB-BED tissue clearing solution.

Imaging acquisition and three-dimensional reconstruction

After embedding the tissues in BB-BED tissue clearing solution, three-dimensional images were captured with a confocal microscope (Leica SP8). The epithelium of *K14-Cre;Ai14* reporter mice was imaged using an Alexa Fluor 555 signal. A 20×/0.95NA objective (Leica; 11507702, 20×/0.95, IMM incl BABB, working distance: 1.95 mm) was used for the study. Image stacks were acquired at a resolution of 1024 × 1024 pixels (pixel size 0.722 µm) with a *z*-step of 1.5 µm. Stitching of tile images in the XY direction was performed using Leica image processing software, while stitching of image stacks in the Z direction was performed using the BigStitcher ImageJ plug-in. The stitching between adjacent tiles and between image stacks utilized a 10% image overlap. Finally, all raw image data were exported in TIFF format. The Imaris File Converter 9.0 software (Bitplane) was used to convert the images from TIFF format to Imaris format. Three-dimensional ren-

dering of the image stacks and subsequent analysis were performed using Imaris 10.1 software. Snapshots were generated using the "Snapshot" function.

Quantitative analysis of the ERM

The number of clusters, the average distance to the five nearest neighbors, the average area, and the average volume of ERM were analyzed using the Imaris 10.1 software. The region of interest (ROI) was defined as the molar region, with only the ERM portion included in the analysis. Quantification of the number of clusters, average area, and average volume of the selected ERMs utilized the "Surface" and "Statistics" functions. The average distance to the five nearest neighbors of the selected ERMs was quantified using the "Surface", "Surface Center of Mass", and "Statistics" functions provided by the software.

Quantitative analysis of HERS

The mesiodistal and buccolingual distances of HERS were analyzed using Imaris 10.1 software. The analysis focused on the cervical and root portions of the molars, specifically targeting the region occupied by HERS. The "Measurement Points" function of the software was used to mark the most concave points on the mesiodistal and distal parts of HERS to measure the mesiodistal distance of HERS. The distances were then quantified using the "Statistics" function. Similarly, for the buccolingual distance, the most prominent points on the buccal and lingual parts were marked using the "Measurement Points" function, and the buccolingual distances were obtained using the "Statistics" function. The mesiodistal and buccolingual growth rates of HERS were calculated by dividing the respective (mesiodistal or buccolingual) distance of HERS by the time period.

Quantitative analysis of the length and elongation direction of continuous HERS

The length and elongation direction of continuous HERS were analyzed using the Imaris 10.1 software. We focused on the cervical and root areas of molars and specifically isolated the region containing HERS for analysis. The structure of continuous HERS was initially identified using the "Surface" function to measure the length of continuous HERS. Next, the endpoints along the longitudinal axis of the tooth root were marked using the "Measurement Points" function, and the length was calculated using the "Statistics" function. To determine the elongation direction of HERS, the angle between the front edge of HERS and the horizontal plane was quantified using the "Measurement Points" and "Statistics" functions available in the software.

Statistical analysis

All data were presented as the mean ± SD along with corresponding 95% confidence intervals (CIs). Statistical significance was assessed using Student's t-test. Difference was considered to be statistically significant at $P < 0.05$. All statistical analyses were conducted using GraphPad Prism and Microsoft Excel.

Results

MiniTESOS tissue clearing method renders the mandible of K14-Cre;Ai14 mice transparent while effectively preserving its endogenous fluorescence

To achieve precise spatial imaging of mouse embryonic and early postnatal mandibles, we used advanced tissue clearing technology. Our experimental workflow included sample collection, tissue clearing, confocal microscopy imaging, and subsequent analysis of the image data (**Figure 1A**). Considering the specific characteristics of mouse embryonic and early postnatal mandibles, such as their low pigmentation, high tissue moisture content, and fragile texture of tissues, we optimized the sample processing time using the TESOS technique and standardized the protocol. This improved tissue clearing approach is known as miniTESOS.

The miniTESOS protocol for mandible samples from *K14-Cre;Ai14* mice involved several steps: fixation (3 h), decalcification (30 min to 3 days for mineralized tissue), decolorization (30 min), delipidation (30 min), dehydration (20 min), and immersion in the clearing solution (1 h). Subsequently, the samples were transformed into transparent blocks with a refractive index of 1.56 using UV light-induced polymerization (**Figure 1B**). Processing of embryonic samples was completed within 5 h, while postnatal sam-
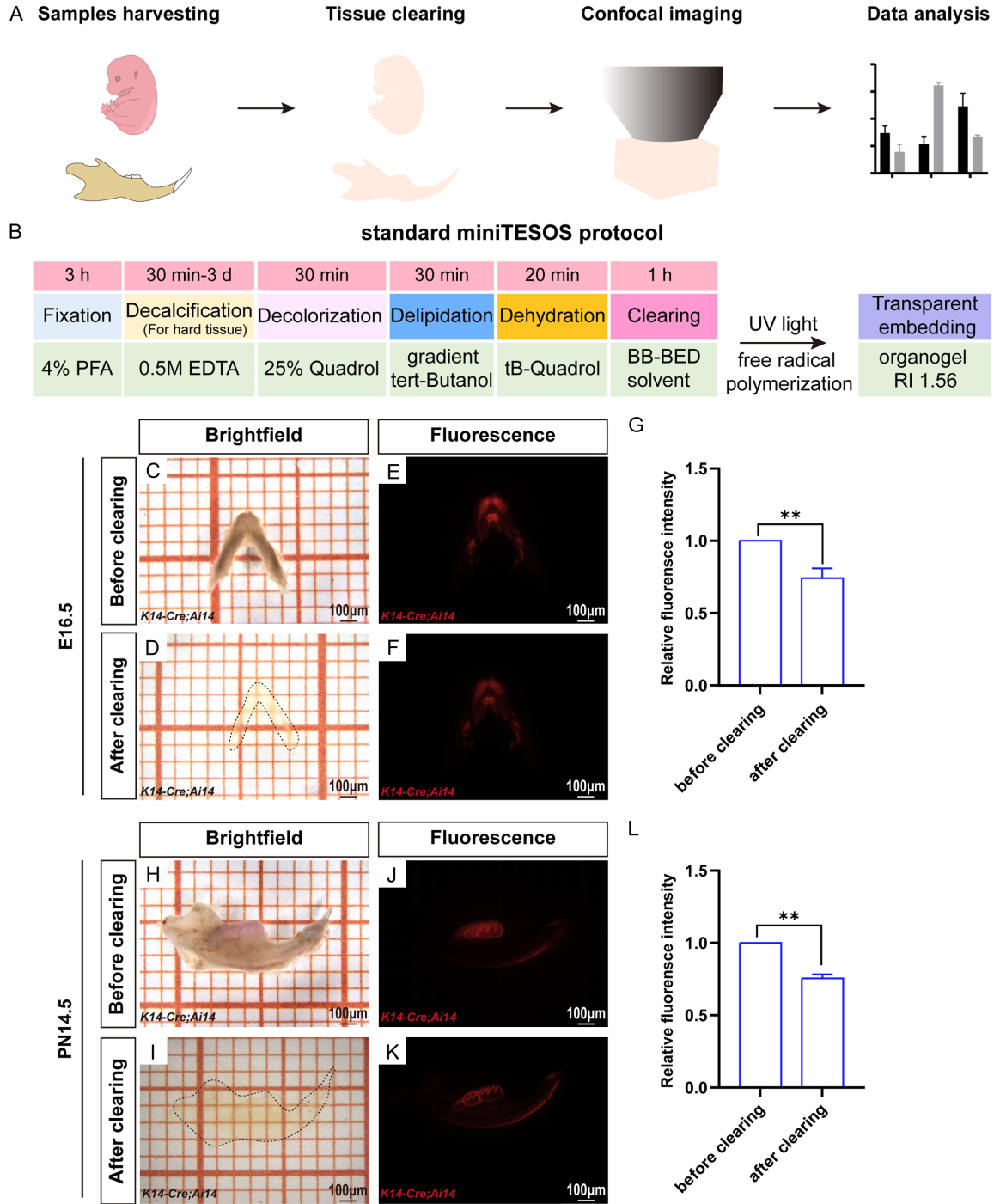
Figure 1. The miniTESOS tissue clearing method renders the mandible of *K14-Cre;Ai14* mice transparent. A. Experimental workflow of the miniTESOS organizational transparency process. B. Procedures of the standard miniTESOS protocol. C, D. Bright-field images of the mandible of *K14-Cre;Ai14* mice at E16.5 before and after transparency using the miniTESOS method. E, F. Fluorescence images of the mandible of *K14-Cre;Ai14* mice at E16.5 before and after transparency using the miniTESOS method. G. Quantification of fluorescent protein brightness before and after clearing the mandible of *K14-Cre;Ai14* mice at E16.5. H, I. Bright-field images of the mandible of *K14-Cre;Ai14* mice at PN14.5 before and after transparency using the miniTESOS method. J, K. Fluorescence images of the mandible of *K14-Cre;Ai14* mice at PN14.5 before and after transparency using the miniTESOS method. L. Quantification of fluorescent protein brightness before and after clearing the mandible of *K14-Cre;Ai14* mice at PN14.5; scale bars: 100 μm. The values are presented as the mean ± SD; $**P < 0.01$; n = 3 per group.

ples required up to four days for completion of processing.

Following miniTESOS clearing, the mandibles of *K14-Cre;Ai14* mice at E16.5 became nearly transparent and were barely visible (**Figure 1C** and **1D**). The fluorescence intensity of the Ai14 fluorescent protein was maintained at over 70% of its original intensity post-clearing (**Figure 1E-G**). Similarly, after miniTESOS treatment, the mandibles of PN14.5 *K14-Cre;Ai14* mice also became nearly transparent and barely visible (**Figure 1H** and **1I**). The fluorescence intensity post-clearing remained above 70% of the original intensity compared to pre-clearing levels (**Figure 1J-L**). Mandibles from additional embryonic stages and early postnatal periods also exhibited similar transparency, maintaining more than 70% of their native fluorescence (data not presented). These results highlighted the effectiveness of the standardized miniTESOS method in preserving sample transparency and fluorescence, facilitating the study of tooth epithelial tissues across diverse developmental stages using advanced three-dimensional imaging techniques.

Three-dimensional morphological observation of the tooth germ at the bud, cap, and bell stages in K14-Cre;Ai14 mice

During the embryonic stage, MM1 sequentially undergo the bud stage (E13.5), cap stage (E15.5), and bell stage (E16.5), during which mineralization has not yet begun. To explore the ability of miniTESOS tissue clearing technology to obtain three-dimensional images of tooth germs during non-mineralized stages, mandibular samples from *K14-Cre;Ai14* mice at the E13.5, E15.5, and E16.5 stages were collected. Following the standardized miniTESOS protocol for mandibular samples, we performed confocal fluorescence microscopy imaging on the molar regions of mouse mandibles.

Figure 2A presents a comprehensive three-dimensional view of MM1 in the mouse mandible at the E13.5 stage. The molar epithelial tissue exhibited localized swelling morphology in both horizontal and sagittal directions (**Figure 2A1**, **2A2**). In the three-dimensional coronal view, we found that at this stage, the MM1 epithelium formed circular or elliptical buds, characterized by a distinct "bud" morphology (**Figure 2A3**). Cross-sections in the horizontal,

sagittal, and coronal planes revealed that during the bud stage, the MM1 epithelium extended downward into the mesenchyme as localized swellings (**Figure 2B-D**).

At the E15.5 stage, MM1 entered the cap stage. The three-dimensional coronal view depicted the distinctive "cap" morphology of MM1 during this time (**Figure 2E** and **2E3**). During this stage, the dental epithelium folded at the apex, forming the characteristic "cervical loop" structure (**Figure 2E3**). MM2 appeared distally relative to MM1 (**Figure 2E2**). In the horizontal, sagittal, and coronal three-dimensional views, clusters of epithelial cells with intense fluorescence marked the location of the primary enamel knot (**Figure 2E1-E3**). The horizontal cross-section showed the primary enamel knot centrally in the MM1 epithelium (**Figure 2F**), while in the sagittal and coronal sections, it was positioned at the base of the epithelium (**Figure 2G** and **2H**).

At the E16.5 stage, MM1 continued to grow and progressed into the bell stage of development. In the three-dimensional coronal view, MM1 displayed a distinct "bell" morphology, with the dental crown features becoming increasingly pronounced. At this stage, the dental epithelium folded at the tip of the future cusps (**Figure 2I**), marking the development of the bell stage (**Figure 2I3**). By analyzing the horizontal, sagittal, and coronal three-dimensional views, we identified two clusters of epithelial cells with high fluorescence intensity, indicating the presence of secondary enamel knots (**Figure 2I1-I3**). The horizontal and coronal cross-sections confirmed that these secondary enamel knots were situated on the buccal and lingual sides, respectively, corresponding to the locations of future cusps (**Figure 2J** and **2L**). Both secondary enamel knots were positioned at the base of the epithelium (**Figure 2K** and **2L**). These spatial and sectional observations highlighted the efficacy of miniTESOS tissue clearing technology in rendering mandibular tissues of *K14-Cre;Ai14* mice transparent during embryonic stages, facilitating their three-dimensional imaging to observe molar morphology at various developmental stages. This indicated the utility of the miniTESOS technique in providing spatial images for research on embryonic tissue development and analyzing cellular-level changes in tissue morphology.
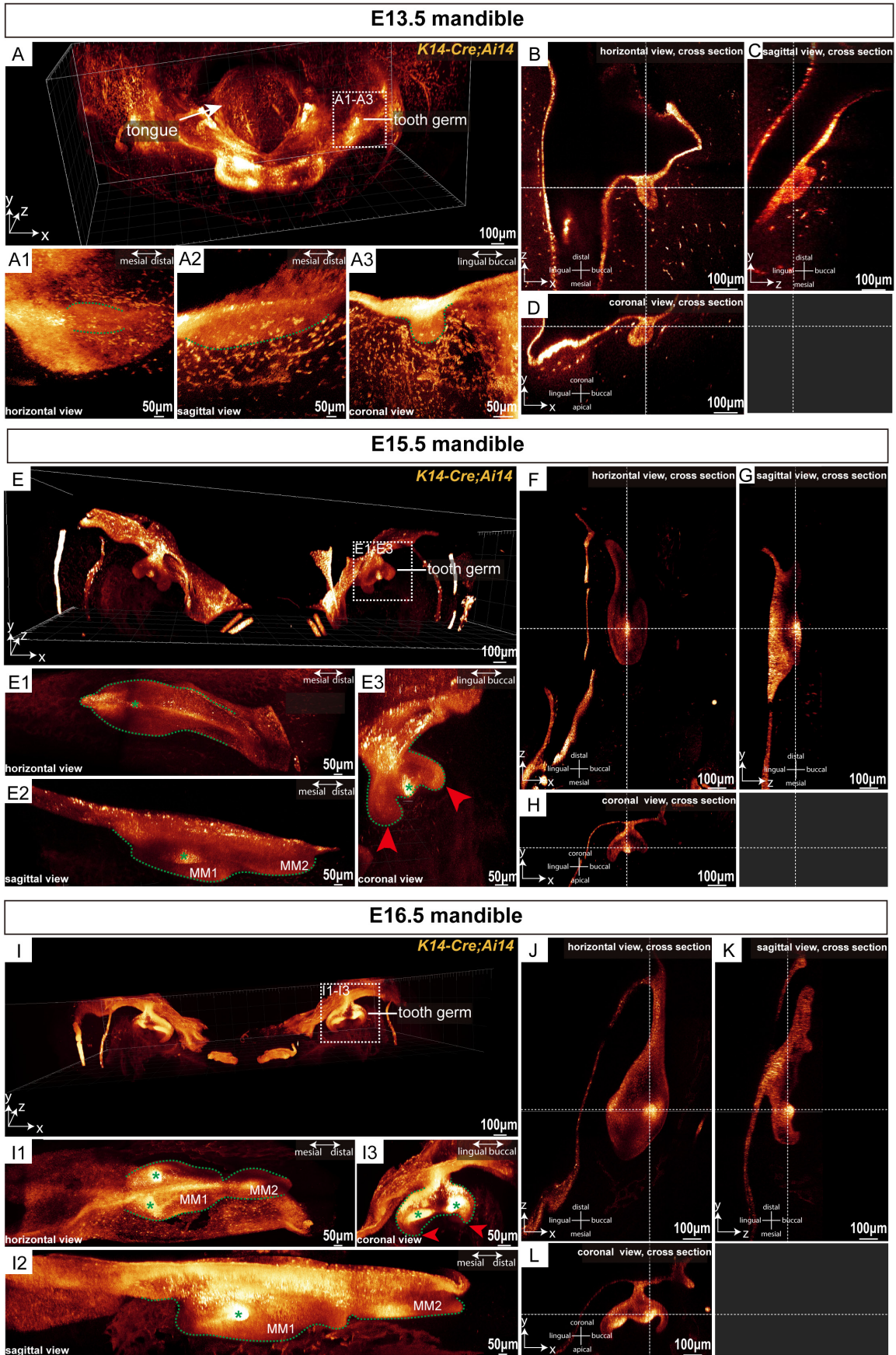
3D visualization of HERS with miniTESOS

Figure 2. MiniTESOS clearing-based deep three-dimensional imaging enables imaging of tooth germ morphology at embryonic stages with high resolution. (A) A three-dimensional view of the mandible from *K14-Cre;Ai14* mice at E13.5; scale bars: 100 µm. (A1-A3) The mouse molar tooth germ at E13.5 is shown in three dimensions. (A1) represents the horizontal view. (A2) represents the sagittal view. (A3) represents the coronal view; scale bars: 50 µm. The green dashed lines circle the outline of the tooth germ. (B-D) MM1 is shown in the horizontal, sagittal, and coronal cross sections, respectively, at E13.5. The white horizontal dashed lines indicate the sections on the same coronal plane, whereas the white vertical dashed lines indicate the sections on the same sagittal plane; scale bars: 100 µm. (E) A three-dimensional view of the mandible of *K14-Cre;Ai14* mice at E15.5; scale bars: 100 µm. (E1-E3) The mouse molar tooth germ at E15.5 is shown in three dimensions. (E1) represents the horizontal view, (E2) represents the sagittal view, and (E3) represents the coronal view; scale bars: 50 µm. The green dashed lines circle the outline of the tooth germ. Red arrowheads show the cervical loop. The green asterisk shows the primary enamel knot; scale bars: 100 µm. (F-H) Horizontal, sagittal, and coronal cross-sections of MM1 at E15.5. The white horizontal dashed lines indicate sections on the same coronal plane, while the white vertical dashed lines indicate sections on the same sagittal plane; scale bars: 100 µm. (I) Three-dimensional view of the mandible from *K14-Cre;Ai14* mice at E16.5; scale bars: 100 µm. (I1-I3) Three-dimensional views of the mouse molar tooth germ at E16.5 are shown in three dimensions. (I1) shows the horizontal view, (I2) shows the sagittal view, and (I3) shows the coronal view; scale bars: 50 µm. Green dashed lines outline the tooth germ. Red arrowheads indicate the cervical loop. Green asterisks denote the second enamel knots. (J-L) Horizontal, sagittal, and coronal cross sections of MM1 at E16.5. The white horizontal dashed lines indicate sections on the same coronal plane, and the white vertical dashed lines indicate sections on the same sagittal plane. MM1, mandibular first molar; MM2, mandibular second molar; scale bars: 100 µm; *n* = 3 per group.

Age-related increase in ERM dispersion in K14-Cre;Ai14 mice revealed by transparent adult mouse teeth

To investigate age-related morphological changes in ERM in adult mice, we collected mandibles from one-month-old and five-month-old *K14-Cre;Ai14* mice. We evaluated the efficacy of the TESOS clearing technique for three-dimensional imaging of mineralized teeth in adult mice (**Figure 3**). At the root of mandibular MM1 in both age groups, ERM appeared as clusters of cells (**Figure 3A** and **3B**), forming a network structure resembling a fishing net around the roots (**Figure 3A1** and **3B1**). This result confirmed that the TESOS clearing technique enables transparent three-dimensional imaging of mineralized teeth, including their hard tissue structures.

The total number of ERM clusters in MM1 was quantified at one month and five months of age. In one-month-old mice, the total number of ERM clusters was 2958.00±150.20. By five months of age, this number significantly decreased to 490.30±85.17 (**Figure 3C**), indicating a significant decrease in ERM clusters with age. Additionally, we measured and statistically analyzed the average distance from each ERM cluster to its five nearest neighboring clusters in both age groups. The average distance between each ERM cluster and its five nearest neighbors significantly increased in the five-month-old mice compared to the one-month-old mice (**Figure 3D**), suggesting a sparser spatial distribution of ERM clusters in the five-month-old mice.

Using three-dimensional spatial images of MM1, we quantified the average surface area and volume of the ERM clusters in the entire molar. In one-month-old mice, the average surface area was 398.80±20.00 µm^2, and the average volume was 477.90±90.51 µm^3. In five-month-old mice, the average surface area was 4582.00±107.50 µm^2, and the average volume was 14312.00±667.50 µm^3 (**Figure 3E** and **3F**). Statistical analysis revealed a significant increase in both the average surface area and volume of ERM clusters in five-month-old mice compared to those in one-month-old mice. These findings suggested that although the number of ERM clusters decreased with age, their surface area and volume increased substantially, which might be related to their role in regulating periodontal tissue regeneration and homeostasis.

Analysis of the growth patterns of HERS in MM1 and MM2 before the fusion of HERS

Both MM1 and MM2 in mice are two-rooted teeth. Despite this similarity, they exhibit significant differences in the rates of hard tissue development and anatomical complexity, as revealed by extensive micro-CT analysis [20, 21]. To investigate these differences further, particularly focusing on variations in the growth of HERS, we conducted systematic three-dimensional imaging using a clearing technique
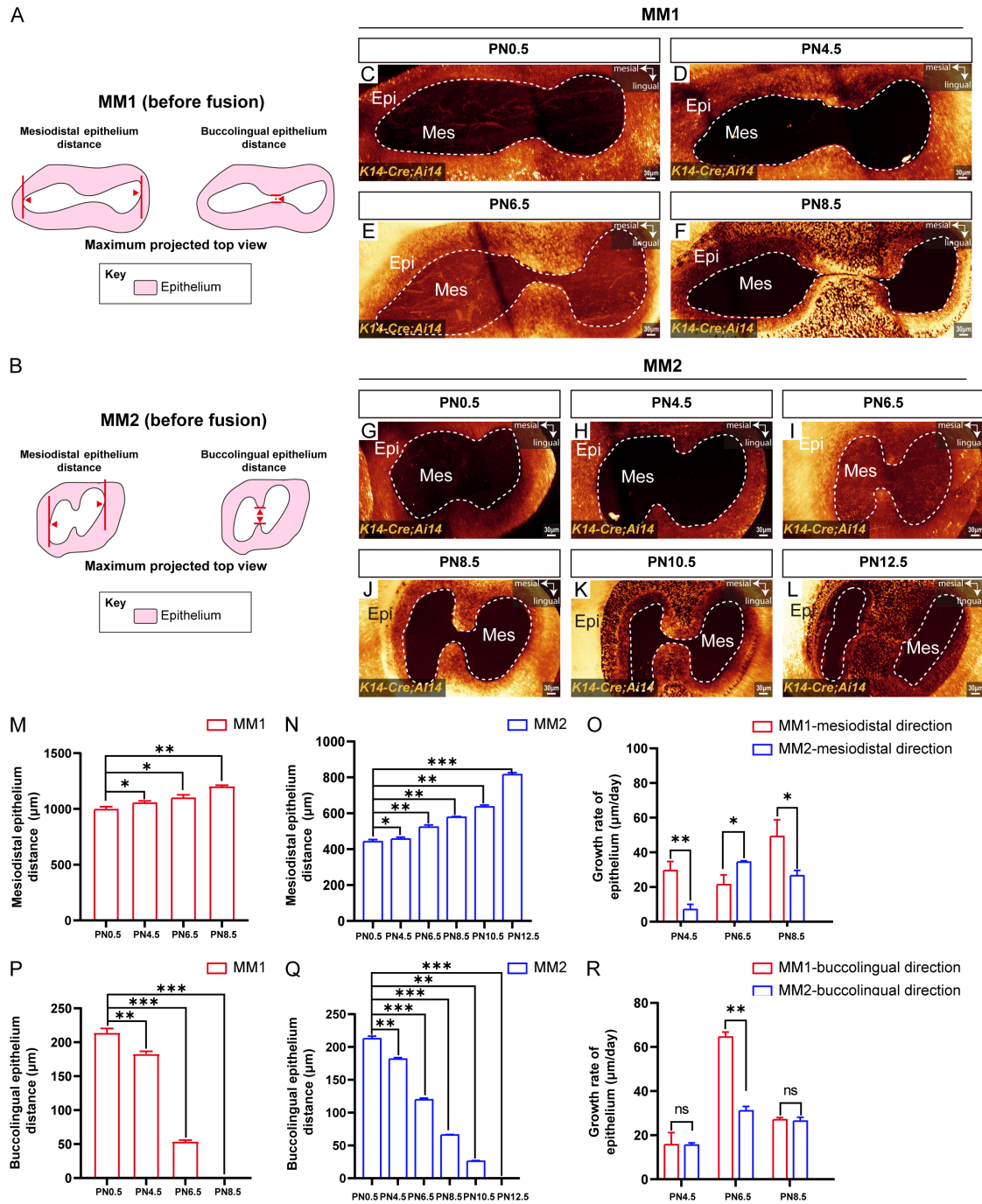
Figure 3. TESOS clearing-based deep three-dimensional imaging enables imaging of hard tissues of adult mouse molars. (A, B) Three-dimensional holistic views of the mandible from *K14-Cre;Ai14* mice at one month and five months, respectively; scale bars: 300 µm. (A1, B1) Higher magnification images of representative ERM clusters within the white dashed boxes in (A, B); scale bars: 100 µm. (C-F) Bar graphs illustrating the number of ERM clusters, average distance to the five nearest neighbors, average area, and average volume, respectively. The values are presented as the mean ± SD; **$P < 0.01$ and ***$P < 0.001$; $n = 3$ per group.

on MM1 and MM2 of *K14-Cre;Ai14* mice from PN0.5 to PN14.5. We measured the distances between HERS in the mesiodistal and buccolingual directions in MM1 and MM2 before the fusion of HERS (**Figure 4A** and **4B**) and subsequently quantified the dynamic developmental patterns. Our findings indicated that from PN0.5 to PN6.5, the buccolingual HERS of MM1 did not fuse (**Figure 4C-E**). By PN8.5, the fusion of the buccolingual HERS of MM1 began (**Figure 4F**). In contrast, the buccolingual HERS of MM2

fused significantly later, at PN12.5 (**Figure 4G-L**), indicating delayed fusion compared to MM1.

To further elucidate the growth patterns of HERS in MM1 and MM2 before their fusion, we measured the distances between HERS in the mesiodistal and buccolingual directions using three-dimensional imaging. Our analysis revealed that the mesiodistal distance of HERS in MM1 increased gradually from 1005.00±4.51

Figure 4. Three-dimensional imaging quantification revealed the growth rate of MM1 and MM2 HERS cells before postnatal fusion. (A, B) Schematic diagrams of the methods used to measure the MM1 and MM2 mesiodistal HERS distances and buccolingual HERS distances. (C-F) Maximum projected top views of M1 from *K14-Cre;Ai14* mice at PN0.5 (C), PN4.5 (D), PN6.5 (E), and PN8.5 (F). (G-L) Maximum projected top views of MM2 from *K14-Cre;Ai14* mice at PN0.5 (G), PN4.5 (H), PN6.5 (I), PN8.5 (J), PN10.5 (K), and PN12.5 (L). (M) Bar graphs showing the mesiodistal distance of HERS from MM1 at PN0.5, PN4.5, PN6.5, and PN8.5. (N) Bar graphs illustrating the mesiodistal distance of HERS from MM2 at PN0.5, PN4.5, PN6.5, PN8.5, PN10.5, and PN12.5. (O) Bar graphs displaying the mesiodistal growth rate of HERS from MM1 and MM2 at PN4.5, PN6.5, and PN8.5. (P) Bar graphs depicting the buccolingual distance of HERS from MM1 at PN0.5, PN4.5, PN6.5, and PN8.5. (Q) Bar graphs showing the buccolingual distance of HERS from MM2 at PN0.5, PN4.5, PN6.5, PN8.5, PN10.5, and PN12.5. (R) Bar graphs illustrating the buccolingual growth rate of HERS from MM1 and MM2 at PN4.5, PN6.5, and PN8.5. The white dashed lines outline the margin of HERS. Epi, epithelium; Mes, mesenchyme; MM1, mandibular first molar; MM2, mandibular second molar; scale bars: 30 μm. The data are presented as the mean ± SD; *$P < 0.05$, **$P < 0.01$, and ***$P < 0.001$; ns indicates not significant; $n = 3$ per group.

μm at PN0.5 to 1205.00±8.18 μm at PN8.5 (**Figure 4M**). In MM2, the mesiodistal distance of HERS increased from 442.00±2.66 μm at PN0.5 to 793.30±2.08 μm at PN12.50 (**Figure 4N**). This indicates that before HERS fusion, both MM1 and MM2 exhibited elongation in the mesiodistal direction, with MM1 consistently showing a longer mesiodistal distance compared to MM2. Next, we analyzed the changes in growth rates in this direction and found that in MM1, the growth rates of mesiodistal HERS were 27.33±3.52 μm/day from PN0.5 to PN4.5 and 49.17±4.75 μm/day from PN6.5 to PN8.5 (**Figure 4O**). In MM2, the growth rates of mesiodistal HERS were 7.32±0.22 μm/day and 26.5±3.12 μm/day during the same periods (**Figure 4O**). This indicates that during these stages, MM1 exhibited a faster growth rate of HERS in the mesiodistal direction compared to MM2. Notably, from PN4.5 to PN6.5, the growth rate of HERS in MM1 was about half that of MM2, indicating a period where MM1 exhibited slower growth compared to MM2 (**Figure 4O**). Overall, the mesiodistal distances of HERS in both MM1 and MM2 continued to increase before their fusion, which might be related to the overall increase in root diameter in this direction. However, their growth rate trends were opposite, potentially reflecting distinct growth dynamics associated with the coordinated development of MM1 and MM2 in mandibular structures.

Simultaneously, the buccolingual distance of HERS in both MM1 and MM2 decreased gradually. At PN8.5 and PN12.5, the buccolingual distance of HERS in MM1 and MM2 was zero, respectively, indicating a complete fusion of HERS in the buccolingual direction (**Figure 4P** and **4Q**). Statistical analysis of the growth rate of HERS in the buccolingual direction revealed that between PN4.5 and PN6.5, MM1 exhibited a growth rate of 64.50±2.29 μm/day, whereas MM2 showed a growth rate of 31.10±2.01 μm/day (**Figure 4R**). The growth rate of MM1 was twice that of MM2, and MM1 reached its peak growth rate before HERS fusion (**Figure 4R**). These findings indicated the critical role of the PN4.5 to PN6.5 period in the buccolingual fusion process of HERS in MM1, contributing the largest growth distance during this phase. There were differences in the growth rates and developmental patterns of MM1 and MM2 in both mesiodistal and buccolingual directions

before HERS fusion at PN8.5 and PN12.5, respectively. Understanding these variations is essential when using MM1 and MM2 as biological models for investigating the molecular mechanisms underlying tooth development and associated diseases.

Gradual reduction in continuous HERS length with root elongation

We found that HERS plays a crucial role in guiding the formation and elongation of the tooth root in the non-furcation region. Previous studies have indicated that HERS is initially assembled during early root formation and elongation stages, followed by subsequent fragmentation [6]. To investigate the specific process of HERS fragmentation during root elongation, we examined HERS status in *K14-Cre;Ai14* mice during this process after HERS fusion on the buccolingual side of MM1 and MM2. Our findings revealed that in MM1, from PN8.5 to PN14.5 after HERS fusion on the buccolingual side, continuous HERS was present only at the leading edge of root elongation, whereas HERS in the more crownward regions had fragmented (**Figure 5A-D**). Similarly, in MM2, during PN12.5 and PN14.5 following HERS fusion on the buccolingual side, continuous HERS was detected only at the leading edge of root elongation (**Figure 5E** and **5F**).

We then performed three-dimensional measurements of the length of continuous HERS at the leading edge of root elongation for MM1 from PN8.5 to PN14.5 and for MM2 from PN12.5 to PN14.5, as illustrated in **Figure 5G**. These results showed that in the mesial root of MM1, the length of continuous HERS decreased from 144.30±15.14 μm at PN8.5 to 56.93±3.27 μm at PN14.5. Similarly, in the distal root of MM1, the length of continuous HERS decreased from 108.31±9.63 μm at PN8.5 to 35.63±5.68 μm at PN14.5 (**Figure 5H**). Throughout PN8.5, PN10.5, PN12.5, and PN14.5, the length of continuous HERS in the mesial root of MM1 consistently exceeded that in the distal root of MM1 (**Figure 5H**). For MM2, the length of continuous HERS in the mesial root decreased from 50.93±3.52 μm at PN12.5 to 44.43±2.83 μm at PN14.5. In contrast, the length of continuous HERS in the distal root of MM2 decreased from 65.65±3.75 μm at PN12.5 to 55.74±2.13 μm at PN14.5 (**Figure 5I**). At
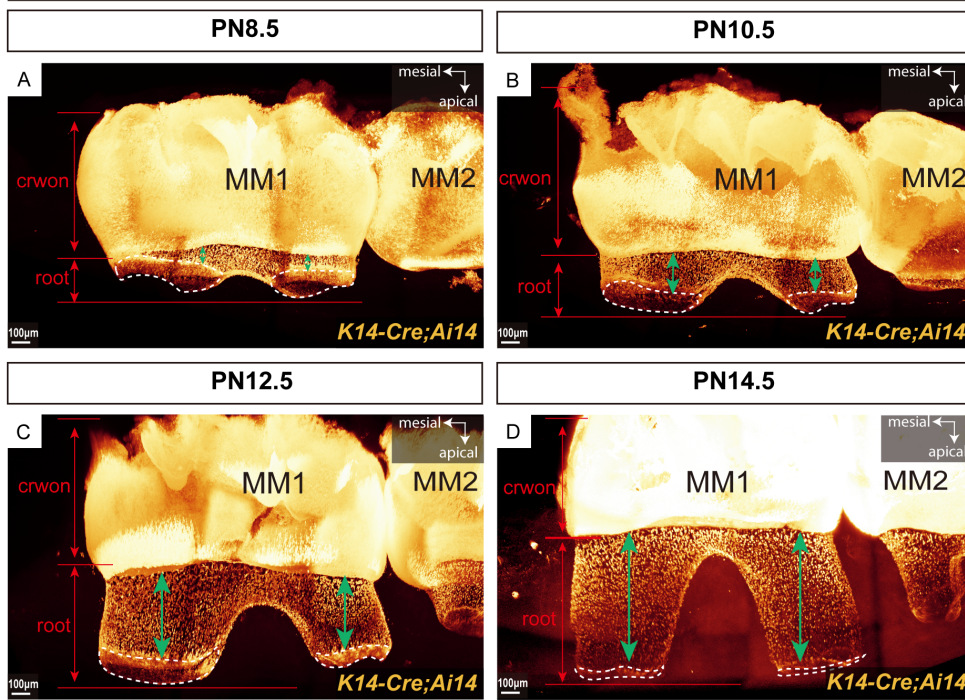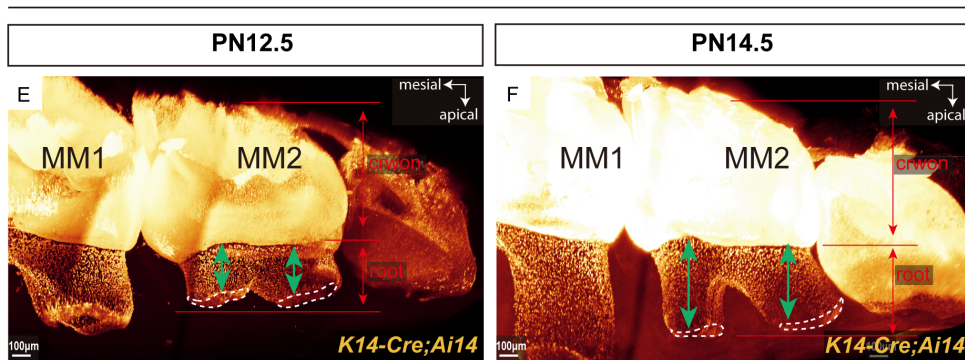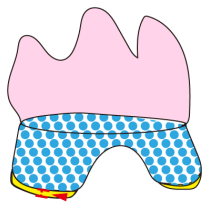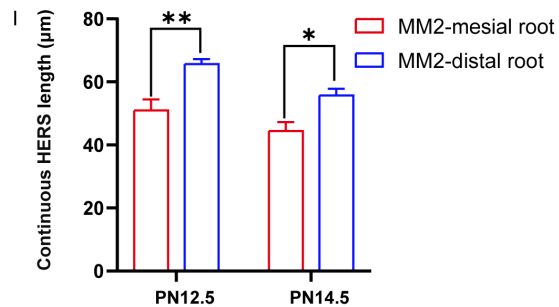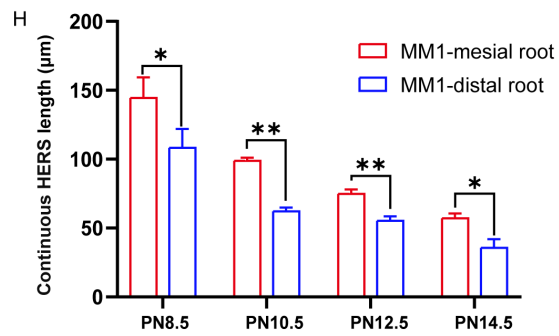
3D visualization of HERS with miniTESOS

Figure 5. Three-dimensional imaging quantification indicated changes in the HERS of MM1 and MM2 during root elongation. (A-D) Three-dimensional view of MM1 from *K14-Cre;Ai14* mice at PN8.5 (A), PN10.5 (B), PN12.5 (C), and PN14.5 (D). (E, F) Three-dimensional view of MM2 from *K14-Cre;Ai14* mice at PN12.5 (E) and PN14.5 (F). (G) Schematic diagrams of the methods used for measuring the continuous HERS length. (H, I) Bar graphs depicting the continuous HERS length from MM1 (H) and MM2 (I). Green bidirectional arrows show the fragmented HERS of roots. The white dashed lines outline the continuous HERS. MM1, mandibular first molar; MM2, mandibular second molar; scale bars: 100 μm. The data are presented as the mean ± SD; *P < 0.05 and **P < 0.01; *n* = 3 per group.

PN12.5 and PN14.5, the length of continuous HERS in the distal root of MM2 consistently exceeded that in the mesial root of MM2 (**Figure 5H**), which was opposite to the pattern observed in MM1. These findings illustrate that during the root elongation stage of two-rooted teeth, continuous HERS is restricted to the leading edge of root elongation and undergoes progressive shortening as the root extends.

Developmental patterns of continuous HERS in the root furcation region

The fusion of HERS on both buccal and lingual sides is crucial for forming the root furcation in two-rooted teeth [22, 23]. To determine how HERS morphology contributes to this process, we examined the three-dimensional morphology, elongation length, and extension angle of HERS in the root furcation area of MM1 from PN4.5 to PN12.5 in *K14-Cre;Ai14* mice. At PN4.5, the root furcation area of MM1 was still not formed (**Figure 6A**). During this period, the tongue-shaped epithelial protrusions of HERS appeared on the buccal and lingual sides, closely associated with the tooth crown epithelium, forming a continuous structure (**Figure 6B** and **6B1**). In the coronal view, HERS on both sides elongated apically relative to the horizontal line (**Figure 6C** and **6C1**). By PN6.5, HERS on the buccal and lingual sides had not fused, and the root furcation area remained undeveloped (**Figure 6D** and **6E**). The tongue-shaped epithelial protrusions of HERS on both sides extended further toward the opposite side, and fragmentation occurred between the leading edges of these protrusions and the tooth crown epithelium, resulting in fragmented HERS (**Figure 6E1**). The continuous tongue-shaped epithelial protrusions of HERS on the buccal and lingual sides changed their elongation direction to a coronal direction (**Figure 6F** and **6F1**). By PN8.5, the tongue-shaped epithelial protrusions of HERS on the buccal and lingual sides started to fuse, and the outline of the root furcation became visible (**Figure 6G** and **6H**).

Besides the newly formed continuous structure where the buccal and lingual protrusions fused, HERS in other areas of the root furcation mostly fragmented (**Figure 6H1**). When the buccal and lingual tongue-shaped epithelial protrusions met and fused, they arched upward at the leading edge instead of meeting horizontally (**Figure 6I** and **6I1**). By PN12.5, the morphology of the root furcation area became more distinct (**Figure 6J**). At this stage, the buccal and lingual tongue-shaped epithelial protrusions of HERS were fully fused. Continuous HERS was no longer observable in the root furcation area, which now consisted of epithelial remnants (**Figure 6K**, **6K1**, **6L** and **6L1**).

To establish a standardized developmental pattern of HERS on both buccal and lingual sides, we analyzed the comprehensive morphological changes in HERS growth. This included measuring the length of continuous HERS at different developmental stages and determining the angle between the buccal and lingual HERS and the horizontal plane during their elongation and fusion (**Figure 6M**). Statistical analysis indicated that compared to PN4.5, the length of continuous HERS on both sides was significantly shorter at PN6.5 and PN8.5 (**Figure 6N**). By PN12.5, no continuous HERS was observed in the root furcation area. Regarding the direction of elongation of continuous HERS at different stages, buccal and lingual HERS first appeared at PN4.5, with an angle of -18.5°±2.0° between their elongation direction and the horizontal plane. As the buccal and lingual HERS elongated by PN6.5, this angle changed to 16.0°±3.0° (**Figure 6O**). Following their contact and subsequent fusion, the angle between their elongation direction and the horizontal plane continued to increase, indicating a directional change during the growth of continuous HERS. These results highlight the dynamic morphological changes and directional adjustments in HERS during the formation of root bifurcation, which may be necessary for the establishment of root bifurcation.
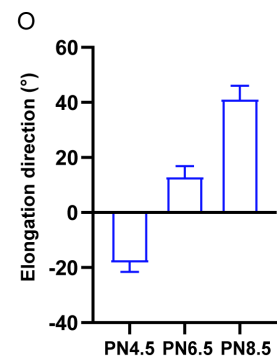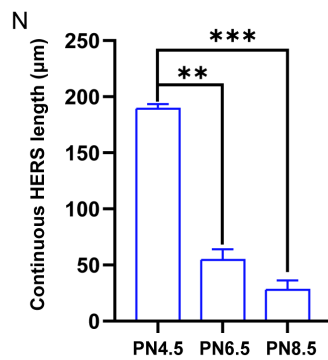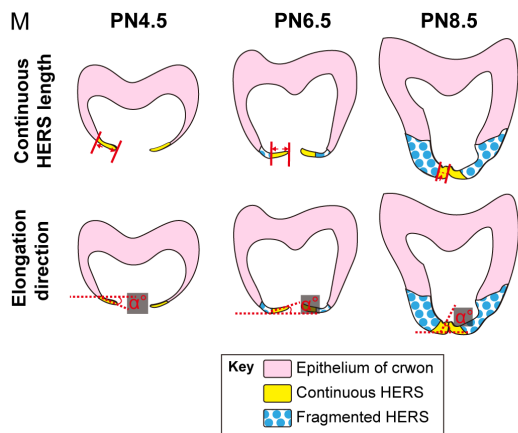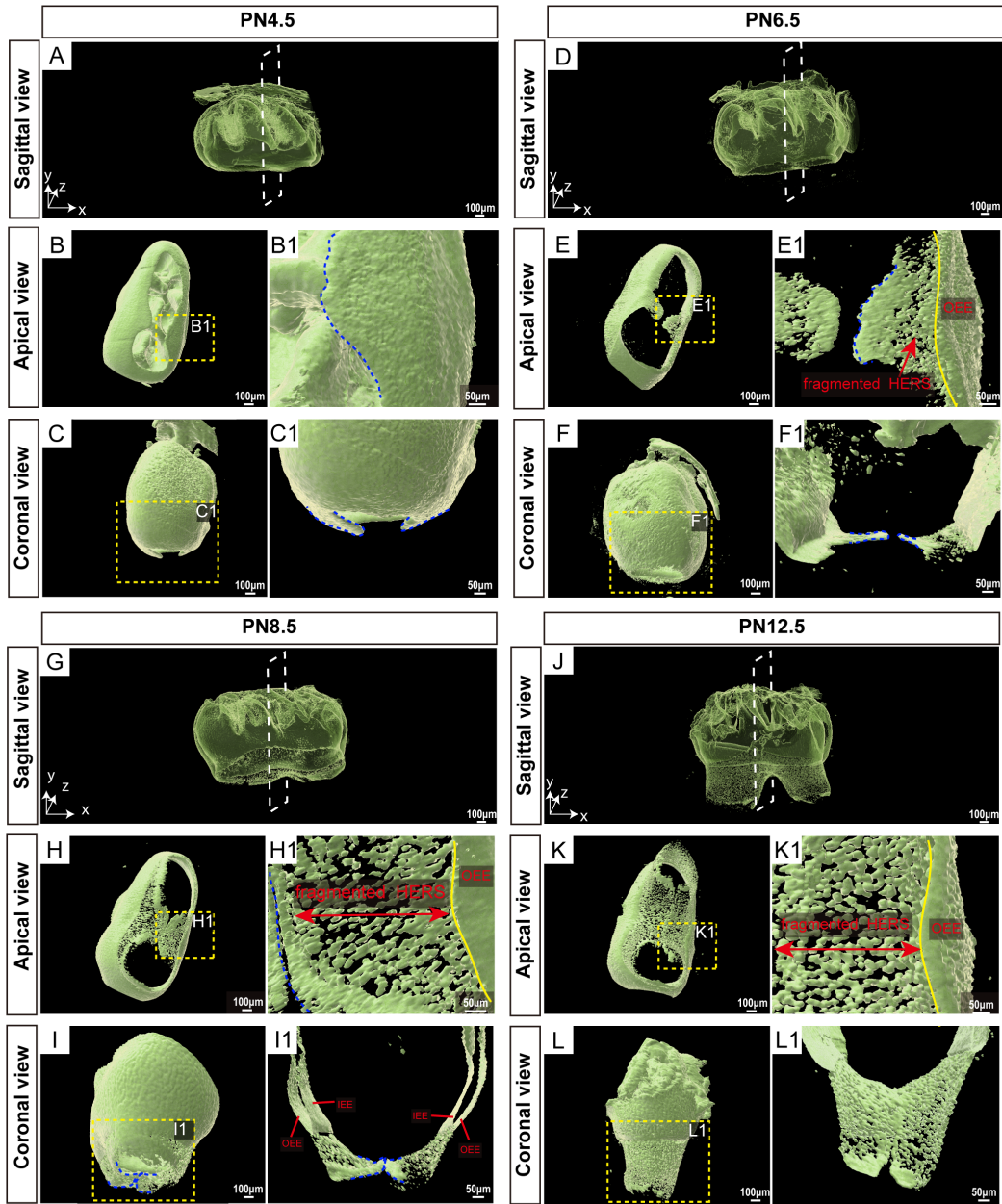
3D visualization of HERS with miniTESOS

Figure 6. Root bifurcation development processes involving HERS in two-rooted teeth. (A-C) At PN4.5, the HERS pattern of MM1 from *K14-Cre;Ai14* mice in the sagittal view (A), apical view (B), and coronal view (C); scale bars: 100 µm. (B1, C1) Higher magnification images of the root bifurcation region of the yellow dashed boxes in (B, C); scale bars: 50 µm. (D-F) At PN6.5, the HERS pattern of MM1 from *K14-Cre;Ai14* mice in the sagittal view (D), apical view (E), and coronal view (F); scale bars: 100 µm. (E1) Higher magnification images of the root bifurcation region of the yellow dashed boxes in (E). The yellow line indicates the dividing line between the OEE of the crown (right side of the yellow line) and the HERS of the root (left side of the yellow line). Red arrowheads show the fragmented part of HERS; scale bars: 50 µm. (F1) Higher magnification images of the yellow dashed boxes in (F), with mesial and distal molar sections removed to expose the protrusions of HERS in the root bifurcation region; scale bars: 50 µm. (G-I) At PN8.5, the sagittal (G), apical (H), and coronal (I) views of the HERS patterns of MM1 from *K14-Cre;Ai14* mice are shown; scale bars: 100 µm. (H1) Higher magnification images of the root bifurcation region of the yellow dashed boxes in (H). The yellow line indicates the dividing line between the OEE of the crown (right side of the yellow line) and the HERS of the root (left side of the yellow line). The red bidirectional arrow line shows the fragmented part of HERS; scale bars: 50 µm. (I1) Higher magnification images of the yellow dashed boxes in (I), with mesial and distal molar sections removed to expose the protrusions of HERS in the root bifurcation region; scale bars: 50 µm. (J-L) At PN12.5, the HERS pattern of MM1 from *K14-Cre;Ai14* mice in the sagittal view (J), apical view (K), and coronal view (L) is shown; scale bars: 100 µm. (K1) Higher magnification images of the root bifurcation region of the yellow dashed boxes in (K). The yellow line indicates the dividing line between the OEE of the crown (right side of the yellow line) and the HERS of the root (left side of the yellow line). The red bidirectional arrow shows the fragmented part of the HERS region; scale bars: 50 µm. (L1) Higher magnification images of the yellow dashed boxes in (L), with mesial and distal molar sections removed to expose the protrusions of HERS in the root bifurcation region; scale bars: 50 µm. (M) Schematic diagrams of the methods used for measuring the continuous HERS length and elongation direction. (N, O) Bar graphs depicting the length and elongation direction of continuous HERS from M1 at PN4.5, PN6.5, PN8.5, and PN12.5. The white dashed box represents the coronal plane, and the blue dashed lines outline the continuous HERS margin in the root bifurcation region. IEE, inner enamel epithelium; OEE, outer enamel epithelium. The data are presented as the mean ± SD; **$P < 0.01$, ***$P < 0.001$; $n = 3$ per group.

Discussion

In clinical settings, abnormalities in HERS often affect the number, length, and shape of tooth roots, leading to dental anomalies such as taurodontism, single-rooted posterior teeth, and root bifurcation malformations [24-26]. The impact of the initial formation of HERS on root development has been extensively studied [27-29], whereas assessment of the subsequent elongation of HERS until complete fragmentation in the development of root bifurcation is limited [30, 31]. We used a tissue clearing technique combined with *K14-Cre;Ai14* transgenic mice to systematically investigate the spatiotemporal changes in HERS from the initiation to elongation stages of two-rooted tooth root development at the cellular level. Through three-dimensional imaging, transient changes in HERS in the root bifurcation region during the formation of root bifurcation were observed. The tissue morphology characteristics of HERS at different periods revealed four developmental stages in the root bifurcation region, including initiation, elongation, contact, and complete fragmentation (**Figure 7**). We summarized the complete developmental pattern of HERS in the root bifurcation region.

Zhao et al. developed the TESOS tissue clearing technique and used it to image the entire body (including the skin) of mouse pups and adult mice, a process that takes more than two weeks [19]. In this study, we refined this technique to create a rapid miniTESOS tissue clearing method that preserves fluorescence compatibility and ensures high tissue transparency. This innovation enabled the swift clearing of mouse mandibles from the embryonic stage to the early postnatal period, achieving tissue transparency within 5 h. Rapid processing is crucial for handling clinical disease tissue samples. Tanaka et al. used tissue clearing techniques to make small tissue blocks from mice and human tumors transparent in two days and revealed various patterns of cancer heterogeneity [32]. The miniTESOS technique developed in this study highlighted the capability of rapidly clearing small-volume tissues and its potential for clinical pathological diagnostics. However, the miniTESOS technique needs to be further tested and optimized for different types and stages of pathological tissues.

Matalova et al. reported that during the development of molar tooth germs, a primary enamel knot forms during the cap stage, followed by the appearance of two secondary enamel knots in the bell stage [33]. These structures play key roles in epithelial signaling throughout tooth germ development [34-36]. Using the miniTESOS tissue clearing technique, we performed
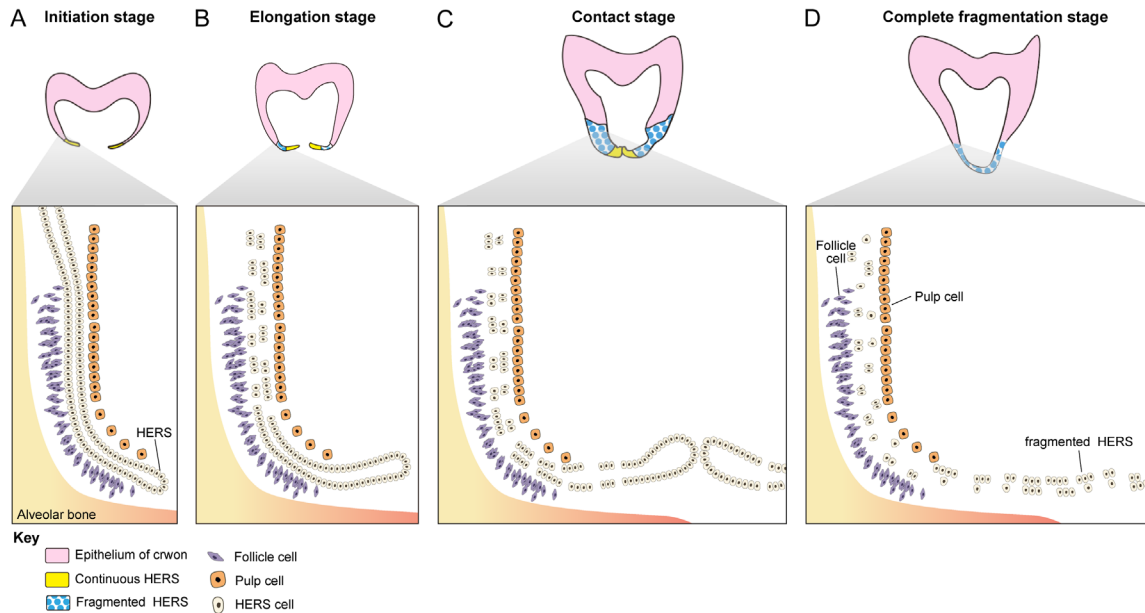
Figure 7. Schematic drawing of the four stages of HERS during the root bifurcation development process. A. Initiation stage: the HERS is oriented toward the apical direction, maintaining structural integrity and continuity with the crown epithelium. B. Elongation stage: the HERS elongates toward the coronal direction and starts to exhibit signs of fragmentation, leading to a disruption of its continuity with the epithelium of the crown. The front edge of the elongation remains continuous. C. Contact stage: the buccolingual HERS begins to fuse, with both the degree and extent of HERS fragmentation increasing. The front edge still maintains its continuity. D. Complete fragmentation stage: the buccolingual sides of HERS are completely fused, and HERS undergoes complete fragmentation.

three-dimensional imaging of *K14-Cre;Ai14* mouse tooth germs at E13.5 (bud stsge), E15.5 (cap stage), and E16.5 (bell stage) with genetic-level resolution. Our results indicated that at the E15.5 and E16.5 stages, the molar tooth germs exhibited one primary enamel knot and two secondary enamel knots in the epithelium, emitting strong fluorescent signals indicative of their role as central points in epithelial signaling. Previous studies have shown the ERM forms a network pattern in the root region and persists throughout the tooth's lifespan following root formation [37-39]. Wang et al. found that the number of ERMs decreases with age due to apoptosis in the molars of Wistar rats and BALB/c mice [40, 41]. Applying the TESOS tissue-clearing technique to one-month-old and five-month-old *K14-Cre;Ai14* mouse molars, we observed significant variations in the number of ERMs across different ages. Three-dimensional imaging further revealed a gradual increase in the volume of ERM clusters over time. Further investigation is needed to understand the physiological implications of these findings.

Before the fusion of HERS, researchers found differences in the characteristics between MM1 and MM2. MM2 exhibits a delayed formation of enamel grooves and enamel knots, along with a consistently narrower enamel organ compared to MM1 [42]. Our findings supported this, showing that before the fusion of buccal and lingual HERS, the mesiodistal distance of HERS was consistently shorter in MM2 than in MM1 in the *K14-Cre;Ai14* mouse model. This discrepancy may be attributed to structural differences in the mandible influencing spatial occupancy along the mesiodistal direction between MM1 and MM2 [43, 44]. We observed similar growth rates of HERS in MM1 and MM2 in the buccolingual direction, peaking between PN4.5 and PN6.5. HERS in MM1 fused at PN8.5, while in MM2, fusion occurred at PN12.5, indicating significant differences in developmental timing. Studies have shown that after fusion, the continuous epithelial structure of HERS closely interacts with newly developing tooth root surfaces [45, 46]. In this study, using the *K14-Cre;Ai14* mouse model, we found continuous HERS only at the apical edge of root elongation in both MM1 and MM2, highlighting its role in promoting apical root elongation. Additionally, Lopez et al. found a decrease in dentin deposition rate as MM1 molar roots elongated [47]. Interestingly, we found a gradu-

al reduction in the length of continuous HERS at the apical edge as molar roots elongated, suggesting a relationship between the length of continuous HERS and the root elongation rate. These findings provided new insights into using MM1 and MM2 as models for investigating tooth development.

Several researchers have attempted to reconstruct segments of MM1 HERS using continuous sectioning methods [40]. In this study, we used tissue clearing technology to systematically analyze morphological changes in HERS during root bifurcation development of MM1 in *K14-Cre;Ai14* mice from PN4.5 to PN12.5. Previous studies have found that in mice, HERS originates from the cervical loop and forms a continuous sheath tightly surrounding the newly developed root surface [4]. As roots elongate, HERS adopts a fragmented, mesh-like morphology covering the root surface [46]. This study comprehensively documented morphological changes in HERS, categorizing them into four stages based on different tissue morphological characteristics: initial, elongation, contact, and complete fragmentation stages. Luan et al. proposed that HERS in mice is a transient and ephemeral structure [6]. Our observations of HERS in the root bifurcation region also revealed transient features. Detailed examination showed that as HERS extended in the root bifurcation area, previously formed HERS structures were interrupted, while newly elongated structures remained continuous. Some researchers have hypothesized that HERS on the buccolingual side of the root bifurcation region extends horizontally from the elongation stage to the contact stage [48]. However, our study found that starting from PN6.5, the HERS on the buccal and lingual sides begins to extend in a coronal direction, forming an angle with the horizontal plane.

To summarize, we developed an efficient and precise miniTESOS tissue clearing method and applied it to the study of tooth development. We found that combining the miniTESOS tissue clearing technique with transgenic reporter mice can be used to precisely study mouse tooth germ development, root development, and HERS development patterns. This method not only advances research on developmental biology but also holds promise for clinical applications in pathological tissues. By visualizing the three-dimensional structures of developing tissues and organs using miniTESOS, we aim to gain deeper insights into their spatiotemporal molecular mechanisms and three-dimensional architecture. This approach provides new strategies and methods for research on tooth regeneration.

Disclosure of conflict of interest

None.

Address correspondence to: Yang Liu and Dong Han, Department of Prosthodontics, Peking University School and Hospital of Stomatology, No. 22 Zhongguancun South Avenue, Haidian District, Beijing 100081, PR China. E-mail: pkussliuyang@bjmu.edu.cn (YL); donghan@bjmu.edu.cn (DH)

References

[1] Yu T and Klein OD. Molecular and cellular mechanisms of tooth development, homeostasis and repair. Development 2020; 147: dev184754.
[2] He YD, Sui BD, Li M, Huang J, Chen S and Wu LA. Site-specific function and regulation of Osterix in tooth root formation. Int Endod J 2016; 49: 1124-1131.
[3] Li J, Parada C and Chai Y. Cellular and molecular mechanisms of tooth root development. Development 2017; 144: 374-384.
[4] Yamamoto H, Cho SW, Kim EJ, Kim JY, Fujiwara N and Jung HS. Developmental properties of the Hertwig's epithelial root sheath in mice. J Dent Res 2004; 83: 688-692.
[5] Yang S, Choi H, Kim TH, Jeong JK, Liu Y, Harada H and Cho ES. Cell dynamics in Hertwig's epithelial root sheath are regulated by β-catenin activity during tooth root development. J Cell Physiol 2021; 236: 5387-5398.
[6] Luan X, Ito Y and Diekwisch TG. Evolution and development of Hertwig's epithelial root sheath. Dev Dyn 2006; 235: 1167-1180.
[7] Zhang S, Li X, Wang S, Yang Y, Guo W, Chen G and Tian W. Immortalized Hertwig's epithelial root sheath cell line works as model for epithelial-mesenchymal interaction during tooth root formation. J Cell Physiol 2020; 235: 2698-2709.
[8] Bouxsein ML, Boyd SK, Christiansen BA, Guldberg RE, Jepsen KJ and Müller R.

Guidelines for assessment of bone microstructure in rodents using micro-computed tomography. J Bone Miner Res 2010; 25: 1468-1486.

[9] Wang Y, Xu R, Luo G and Wu J. Three-dimensional reconstruction of light microscopy image sections: present and future. Front Med 2015; 9: 30-45.

[10] Liu P, Zhang T and Huang Y. Three-dimensional model of normal human dermal tissue using serial tissue sections. Front Bioeng Biotechnol 2024; 12: 1347159.

[11] He C, Yuan Y, Gong C, Wang X and Lyu G. Applications of tissue clearing in central and peripheral nerves. Neuroscience 2024; 546: 104-117.

[12] Mavrovounis G, Skouroliakou A, Kalatzis I, Stranjalis G and Kalamatianos T. Over 30 years of DiI use for human neuroanatomical tract tracing: a scoping review. Biomolecules 2024; 14: 536.

[13] Karthikeyan S, Asakura Y, Verma M and Asakura A. Tissue clearing and confocal microscopic imaging for skeletal muscle. Methods Mol Biol 2023; 2640: 453-462.

[14] Ren G and Pei G. Research progress on three-dimensional reconstruction and visualization of peripheral nerve. Zhongguo Xiu Fu Chong Jian Wai Ke Za Zhi 2009; 23: 239-244.

[15] Jing D, Zhang S, Luo W, Gao X, Men Y, Ma C, Liu X, Yi Y, Bugde A, Zhou BO, Zhao Z, Yuan Q, Feng JQ, Gao L, Ge WP and Zhao H. Author correction: tissue clearing of both hard and soft tissue organs with the PEGASOS method. Cell Res 2019; 29: 506.

[16] Ueda HR, Dodt HU, Osten P, Economo MN, Chandrashekar J and Keller PJ. Whole-brain profiling of cells and circuits in mammals by tissue clearing and light-sheet microscopy. Neuron 2020; 106: 369-387.

[17] Kolesová H, Olejníčková V, Kvasilová A, Gregorovičová M and Sedmera D. Tissue clearing and imaging methods for cardiovascular development. iScience 2021; 24: 102387.

[18] Woo J, Kang H, Lee EY, Park S and Cho YE. Investigation of PRDM7 and PRDM12 expression pattern during mouse embryonic development by using a modified passive clearing technique. Biochem Biophys Res Commun 2020; 524: 346-353.

[19] Yi Y, Li Y, Zhang S, Men Y, Wang Y, Jing D, Ding J, Zhu Q, Chen Z, Chen X, Li JL, Wang Y, Wang J, Peng H, Zhang L, Luo W, Feng JQ, He Y, Ge WP and Zhao H. Mapping of individual sensory nerve axons from digits to spinal cord with the transparent embedding solvent system. Cell Res 2024; 34: 124-139.

[20] Ko DJ, Kelly T, Thompson L, Uppal JK, Rostampour N, Webb MA, Zhu N, Belev G, Mondal P, Cooper DML and Boughner JC. Timing of mouse molar formation is independent of jaw length including retromolar space. J Dev Biol 2021; 9: 8.

[21] Tang Y, Liu C, Wu YH, Pei F and Gu YC. Micro-CT analysis of tooth development of C57BL/6 mice strain. Zhonghua Kou Qiang Yi Xue Za Zhi 2023; 58: 238-243.

[22] Sun K, Yu M, Wang J, Zhao H, Liu H, Feng H, Liu Y and Han D. A Wnt10a-Notch signaling axis controls Hertwig's epithelial root sheath cell behaviors during root furcation patterning. Int J Oral Sci 2024; 16: 25.

[23] Zeichner-David M, Oishi K, Su Z, Zakartchenko V, Chen LS, Arzate H and Bringas P Jr. Role of Hertwig's epithelial root sheath cells in tooth root development. Dev Dyn 2003; 228: 651-663.

[24] Luder HU. Malformations of the tooth root in humans. Front Physiol 2015; 6: 307.

[25] Bharti R, Chandra A, Tikku AP and Wadhwani KK. "Taurodontism" an endodontic challenge: a case report. J Oral Sci 2009; 51: 471-474.

[26] Chetty M, Roomaney IA and Beighton P. Taurodontism in dental genetics. BDJ Open 2021; 7: 25.

[27] Khan M, Seppala M, Zoupa M and Cobourne MT. Hedgehog pathway gene expression during early development of the molar tooth root in the mouse. Gene Expr Patterns 2007; 7: 239-243.

[28] Park JC, Herr Y, Kim HJ, Gronostajski RM and Cho MI. Nfic gene disruption inhibits differentiation of odontoblasts responsible for root formation and results in formation of short and abnormal roots in mice. J Periodontol 2007; 78: 1795-1802.

[29] Rao P, Jing J, Fan Y and Zhou C. Spatiotemporal cellular dynamics and molecular regulation of tooth root ontogeny. Int J Oral Sci 2023; 15: 50.

[30] Li X, Zhang S, Zhang Z, Guo W, Chen G and Tian W. Development of immortalized Hertwig's epithelial root sheath cell lines for cementum and dentin regeneration. Stem Cell Res Ther 2019; 10: 3.

[31] Ide Y, Nakahara T, Nasu M and Ishikawa H. Cell dynamics in Hertwig's epithelial root sheath and surrounding mesenchyme in mice irradiated to the head. Oral Dis 2015; 21: 232-239.

[32] Tanaka N, Kanatani S, Tomer R, Sahlgren C, Kronqvist P, Kaczynska D, Louhivuori L, Kis L, Lindh C, Mitura P, Stepulak A, Corvigno S, Hartman J, Micke P, Mezheyeuski A, Strell C, Carlson JW, Fernández Moro C, Dahlstrand H, Östman A, Matsumoto K, Wiklund P, Oya M, Miyakawa A, Deisseroth K and Uhlén P. Whole-tissue biopsy phenotyping of three-dimension-

al tumours reveals patterns of cancer heterogeneity. Nat Biomed Eng 2017; 1: 796-806.

[33] Matalova E, Antonarakis GS, Sharpe PT and Tucker AS. Cell lineage of primary and secondary enamel knots. Dev Dyn 2005; 233: 754-759.

[34] Thesleff I, Keränen S and Jernvall J. Enamel knots as signaling centers linking tooth morphogenesis and odontoblast differentiation. Adv Dent Res 2001; 15: 14-18.

[35] Mogollón I, Moustakas-Verho JE, Niittykoski M and Ahtiainen L. The initiation knot is a signaling center required for molar tooth development. Development 2021; 148: dev194597.

[36] Lochovska K, Peterkova R, Pavlikova Z and Hovorakova M. Sprouty gene dosage influences temporal-spatial dynamics of primary enamel knot formation. BMC Dev Biol 2015; 15: 21.

[37] Rincon JC, Young WG and Bartold PM. The epithelial cell rests of Malassez--a role in periodontal regeneration? J Periodontal Res 2006; 41: 245-252.

[38] Bykov VL. Epithelial cell rests of Malassez: tissue, cell, and molecular biology. Morfologiia 2003; 124: 95-103.

[39] Becktor KB, Nolting D, Becktor JP and Kjaer I. Immunohistochemical localization of epithelial rests of Malassez in human periodontal membrane. Eur J Orthod 2007; 29: 350-353.

[40] Wang Y, Lv L, Yu X, Zhang T and Li S. The characteristics of epithelial cell rests of Malassez during tooth eruption of development mice. J Mol Histol 2014; 45: 1-10.

[41] Pulitano-Manisagian GE and Mandalunis PM. Epithelial rests of Malassez in experimental animals at different ages. Acta Odontol Latinoam 2021; 34: 3-9.

[42] Lesot H, Hovorakova M, Peterka M and Peterkova R. Three-dimensional analysis of molar development in the mouse from the cap to bell stage. Aust Dent J 2014; 59 Suppl 1: 81-100.

[43] Watson PJ, Fitton LC, Meloro C, Fagan MJ and Gröning F. Mechanical adaptation of trabecular bone morphology in the mammalian mandible. Sci Rep 2018; 8: 7277.

[44] Radlanski RJ, Renz H, Zimmermann CA, Mey R and Matalova E. Morphogenesis of the compartmentalizing bone around the molar primordia in the mouse mandible during dental developmental stages between lamina, bell-stage, and root formation (E13-P20). Ann Anat 2015; 200: 1-14.

[45] Jeong JK, Kim TH, Choi H and Cho ES. Impaired breakdown of Herwig's epithelial root sheath disturbs tooth root development. Dev Dyn 2024; 253: 423-434.

[46] Huang X, Bringas P Jr, Slavkin HC and Chai Y. Fate of HERS during tooth root development. Dev Biol 2009; 334: 22-30.

[47] Gonzalez Lopez M, Huteckova B, Lavicky J, Zezula N, Rakultsev V, Fridrichova V, Tuaima H, Nottmeier C, Petersen J, Kavkova M, Zikmund T, Kaiser J, Lav R, Star H, Bryja V, Henyš P, Vořechovský M, Tucker AS, Harnos J, Buchtova M and Krivanek J. Spatiotemporal monitoring of hard tissue development reveals unknown features of tooth and bone development. Sci Adv 2023; 9: eadi0482.

[48] Jafarzadeh H, Azarpazhooh A and Mayhall JT. Taurodontism: a review of the condition and endodontic treatment challenges. Int Endod J 2008; 41: 375-388.